PAPER

Highly dispersive Co₃O₄ nanoparticles incorporated into a cellulose nanofiber for a high-performance flexible supercapacitor†

Iqra Rabani,[a] Jeseung Yoo,[a] Hyo-Sun Kim,[a] Do Van Lam,[b] Sajjad Hussain, [ID] [a] K. Karuppasamy [ID] [c] and Young-Soo Seo [ID] *[a]

Transition metal oxides used as electrode materials for flexible supercapacitors have attracted huge attention due to their high specific capacitance and surface-to-volume ratio, specifically for cobalt oxide (Co₃O₄) nanoparticles. However, the low intrinsic electronic conductivity and aggregation of Co₃O₄ nanoparticles restrict their electrochemical performance and prevent these electrode materials from being commercialized. Herein, a facile, advantageous, and cost effective sol–gel synthetic route for growing Co₃O₄ nanoparticles uniformly over a low cost and eco-friendly one-dimensional (1D) hydrophilic cellulose nanofiber (CNF) surface has been reported. This exhibits high conductivity, which enables the symmetric electrode to deliver a high specific capacitance of ~214 F g⁻¹ at 1 A g⁻¹ with remarkable cycling behavior (~94% even after 5000 cycles) compared to that of pristine CNF and Co₃O₄ electrodes in an aqueous electrolyte. Furthermore, the binder-free nature of 1D Co₃O₄@CNF (which was carbonized at 200 °C for about 20 min under a H₂/Ar atmosphere) shows great potential as a hybrid flexible paper-like electrode and provides a high specific capacitance of 80 F g⁻¹ at 1 A g⁻¹ with a superior energy density of 10 W h kg⁻¹ in the gel electrolyte. This study provides a novel pathway, using a hydrophilic 1D CNF, for realizing the full potential of Co₃O₄ nanoparticles as advanced electrode materials for next generation flexible electronic devices.

1. Introduction

Electrochemical energy storage (EES) devices, such as lithium ion batteries (LIBs), potassium-ion batteries (PIBs) and supercapacitors (SCs) in a flexible form, have received much attention due to their widespread use in e-readers, mobile phones, smart clothes, transplantable medical devices, displays, electronic skins, tablets, and laptop roll-up display pannels.[1–5] Recently, much work has been dedicated to addressing energy crisis as well as improving the performance of EES devices. Among EES devices, SCs are one of the most promising candidates[6] and have been widely explored because of their low capital cost, fast charge–discharge rate, and extended life cycle.[7,8] SCs are usually categorized into two types on the basis of energy storage mechanism: electrical double layer (EDLC)[9] and pseudocapacitor types.[10] Among them, pseudocapacitors have the benefit of reversible faradaic reactions occurring near the surface of the electrode and exhibiting better storage and electrochemical performance compared to conventional carbon based EDLC.[9] However, in the development of pseudocapacitive materials with theoretical specific capacitance, achieving flexibility and stability remains challenging but will yield more practical values on a commercial scale.[11,12]

Because of their variable electronic structures, high theoretical capacitance, and low cost, transition metal oxides (TMOs), including NiO,[13] ZnO,[14] MnO₂,[15] WO₃,[16] RuO₂,[17] and Co₃O₄,[18,19] have received immense attention as promising flexible electrode materials for SCs based on the conversion reaction mechanism with superior capacitive behavior.[20] However, the low intrinsic electronic conductivity and aggregation phenomena exhibited by TMOs restrict their electrochemical performance in high-performance SCs and prevent their commercialization. To overcome the above-mentioned factors and resolve the global energy crisis, carbon-based materials have been combined with TMOs to prevent aggregation and further boost electrical conductivity and overall electrochemical performance of SC cells.[21–23]

[a]Department of Nanotechnology and Advanced Materials Engineering, Sejong University, Seoul 05006, Republic of Korea. E-mail: ysseo@sejong.ac.kr
[b]Department of Applied Nanomechanics, Korea Institute of Machinery and Materials, Daejeon 34103, Republic of Korea
[c]Division of Electronics and Electrical Engineering, Dongguk University-Seoul, Seoul 04620, Republic of Korea
†Electronic supplementary information (ESI) available. See DOI: 10.1039/d0nr06982e

Among TMOs, eco-friendly, Earth abundant cobalt spinel oxide, Co_3O_4, exhibits a high theoretical specific capacitance of 3560 F g^{-1}, better pseudocapacitive behavior, and environmental friendliness and is considered to be a promising candidate for high performance SCs.[24,25] However, the experimental capacitance obtained for Co_3O_4 thus far does not reach its theoretical capacitance because of sluggish electrical conductivity and restricted electrochemical stability during the galvanostatic charge–discharge process.[26,27] To improve the charge transfer kinetics at the electrode/electrolyte interface, different synthetic approaches and nanostructures of Co_3O_4 have been identified.[28] Among the various nanoarchitecture forms, 1D nanostructures, such as nanobelts, nanoribbons, nanowires, nanotubes, and nanorods, have become a focal area of interest due to their high surface area and better intrinsic electrical conductivity, which together boost capacitive performance compared with their bulk counterparts.[29,30] Furthermore, 1D nanostructure-based electrodes have large and accessible inner and outer surfaces, making them feasible platforms for improving SCs performance through the rapid charge transport of ions.[31,32]

Currently, paper-like flexible devices in all-solid-state supercapacitors are considered promising candidates for energy storage systems as they are safe, eco-friendly, light weight, and easy to handle because they avoid liquid-like electrolytes and can be sufficiently bent, folded, and stretched.[33–36] Therefore, advanced studies are needed to develop a flexible paper-like device with higher capacitive performance and deformation, which remains a difficult goal. According to previous reports, cellulose nanofibers (CNF) can efficiently help the inherent SC performance of reduced graphene oxide and carbon nanotubes because of their 1D nanostructure and hydrophilicity (*i.e.*, dried CNF can easily re-swell in an aqueous electrolyte solution).[34,37,38] This hydrophilic property of 1D CNF can efficiently alleviate the transmission distance of electrolyte ions. 1D CNF can provide multi-channels and mesoporous morphology for transport and absorption of water and key ions through the inner and outer surface of the films. Moreover, 1D CNF possess an appropriate geometric structure (an approximately few microns long and ~3–4 nm wide), including features such as low density, flexibility, and cost effectiveness; they are also an environmentally friendly dispersant of aggregative materials.[38,39]

In this study, we employed a simple and low-cost sol–gel synthesis technique to grow Co_3O_4 nanoparticles on the surface of CNF as a 1D hybrid nanostructure. Hydrophilic CNF enhances the dispersion stability of the Co_3O_4 nanoparticles and reduces internal resistance, facilitating the diffusion of the electrolyte ions to the inner part of the electrode, thereby improving the performance of the SC cell. As a result, this 1D hybrid symmetric supercapacitor (SSC) electrode exhibits high specific capacitance (~214 F g^{-1} at 1 A g^{-1}) and superior cycling stability (~94% over 5000 cycles) in an aqueous electrolyte solution. In addition, a 1D Co_3O_4@CNF hybrid flexible paper electrode was prepared using a vacuum filtration process and carbonized at 200 °C for 20 min in a mixture of H_2/Ar

atmosphere with 10/20 sccm. After carbonization, a 1D Co_3O_4@CNF hybrid can be easily bent and folded due to the continued presence of the cellulose, which delivers a maximum specific capacitance (~80 F g^{-1} at 1 A g^{-1}) along with remarkable energy density (~10 W h kg^{-1} at 0.9 K W kg^{-1}) in the gel electrolyte.

2. Experimental section

2.1. Materials

The anhydrous ethanol (CH_3CH_2OH, 99.5%, M_w = 46.07), Triton X-100 (t-Oct-C_6H_4-$(OCH_2CH_2)_xOH$, M_w = 625) and potassium hydroxide (KOH, 85%, M_w = 56.11) were purchased from Daejung, Korea. Cobalt(II) chloride hexahydrate ($CoCl_2 \cdot 6H_2O$, 98%, M_w = 129.8) was obtained from Junsei, Japan. CNF was donated by Moorim P&P resided in Ulsan, Korea.

2.2. Synthesis of Co_3O_4 nanoparticles on the CNF surface

In a typical synthetic process, 1 g of CNF was dispersed in 200 mL of absolute ethanol in a 500 mL round bottomed flask using a homogenizer for 60 s. The obtained CNF solution was sonicated for 1 h and then kept at 100 °C. Thereafter, 0.9 g of cobalt chloride hexahydrate(II) was added into the CNF solution. Another precursor solution was prepared by mixing Triton X-100 (1%) and KOH (0.3 g) in the same flask. The resultant KOH–Triton solution was transferred to a dropping funnel and added dropwise into the CNF–cobalt solution until the solution became black under vigorous stirring for 2 h at 100 °C. The sample was then allowed slowly to cool to room temperature (RT) for 1 h and further washed and centrifuged (700 rpm, 10 min) using distilled water and ethanol. The sample thus obtained was dried at 100 °C in a convection oven for 12 h. The dried sample was denoted as 1D Co_3O_4@CNF hybrid nanostructure. The 1D Co_3O_4@CNF hybrid powder was further annealed at 200 °C for about 20 min under a H_2/Ar atmosphere with 10/20 sccm. The control sample cobalt oxide nanoparticles were synthesized using a similar procedure without CNF. The prepared samples were kept in a vacuum desiccator for exposure to the moisture.

2.3. Electrochemical tests

For supercapacitive properties of 1D Co_3O_4@CNF hybrid electrodes, cyclic voltammetry (CV), galvanostatic charge–discharge (GCD), and electrochemical impedance spectroscopy (EIS) techniques were conducted using a Biologic SAS (SP-150) workstation in a three-electrode setup at RT. The 1D Co_3O_4@CNF hybrid electrode was used as the working electrode. A platinum wire, a Hg/HgO electrode, and 3 M KOH aqueous solution were employed as the counter electrode, reference electrode and electrolyte, respectively. The working electrode was prepared using the following procedure: active material, carbon black, and polyvinylidene fluoride (PVDF) in stoichiometric ratios (80 : 10 : 10) were mixed in a mortar with N-methyl-2-pyrrolidone (NMP) as the solvent to form the

slurry. Subsequently, the slurry was coated over the nickel (Ni) foam and dried at 120 °C for 12 h to remove excessive solvent. The weight of the active material was ~2 mg, and the area of the electrode was 1 cm^2. The CV and GCD profiles were recorded from −0.2 to +0.6 V at different sweep rates and current densities. EIS analysis was carried out in the frequency range of 1 Hz–200 kHz with an AC signal amplitude of 10 mV. The specific capacitance (C_s) of the single electrode was determined from the GCD profiles using the following equation:

$$C_s = \frac{(I \times \Delta t)}{(m \times \Delta V)} \quad (1)$$

where ΔV is the potential window, Δt is the discharging time, m is the mass of the active electrode material, and I is the loading current density.[40]

2.4. Fabrication of the symmetric device

For practical applications, the SSC for the 1D Co$_3$O$_4$@CNF hybrid as a positive and negative electrode with a similar active weight was prepared. The active material coating on Ni foam is described in the previous section. The two electrodes were attached to a Ni sheet, which was used as the current collector. A rectangular slice of the separator was dipped into the 3 M KOH solution for a few minutes. Thereafter, a separator was attached between these two identical electrodes to form a sandwich-like fabrication which was then sealed with a laminating sheet by applying appropriate pressure. CV and GCD measurements were recorded between 0 and 1 V at different sweep rates and current densities. EIS analysis was carried out in the frequency range between 1 Hz and 200 kHz with an AC signal amplitude of 10 mV. The C_s, energy density (E), power density (P) and coulombic efficiency % (η) of SSC cells were determined using the following equation:

$$C_s = \frac{(2 \times I \times \Delta t)}{(m \times \Delta V)} \quad (2)$$

$$E = \frac{C_s \times (\Delta V)^2}{8} \quad (3)$$

$$P = \frac{(3600 \times E)}{\Delta t} \quad (4)$$

$$\eta = \frac{\Delta t_d}{\Delta t_c} \times 100 \quad (5)$$

where ΔV is the voltage window, Δt is the discharge time, m is the mass of the active electrode material, and I is the loading current density.[41]

2.5. Fabrication of the flexible symmetric device

The schematic illustration of the 1D Co$_3$O$_4$@CNF flexible paper like film is shown in Scheme 1. The resulting flexible paper like film carbonized about 20 min at 200 °C in a gas mixture of H$_2$/Ar with 10/20 sccm. The flexible paper like film was allowed to cool until it reached the ambient atmospheric temperature and then this film was utilized as an working electrode. The flexible paper like electrode area was 1 × 1 cm^2 and the weight was 6 mg. Finally, the PVA–KOH polymer gel electrolyte was sandwiched between the two identical 1D Co$_3$O$_4$@CNF flexible paper like electrodes with silver wires to fabricate the flexible SSC device. Briefly, the PVA–KOH gel was prepared by dissolving 1.0 g of PVA in 25 mL of water on the hot plate at 90 °C. The separately prepared KOH solution (1 g of KOH in 10 mL of water) was then drop wisely added into the PVA solution under continuous stirring until the gel was clear. The whole PVA–KOH gel electrolyte's preparation was carried out at room temperature. The C_s, E, and P values of the flexible SSC cells were determined using eqn (4), (5) and (6).
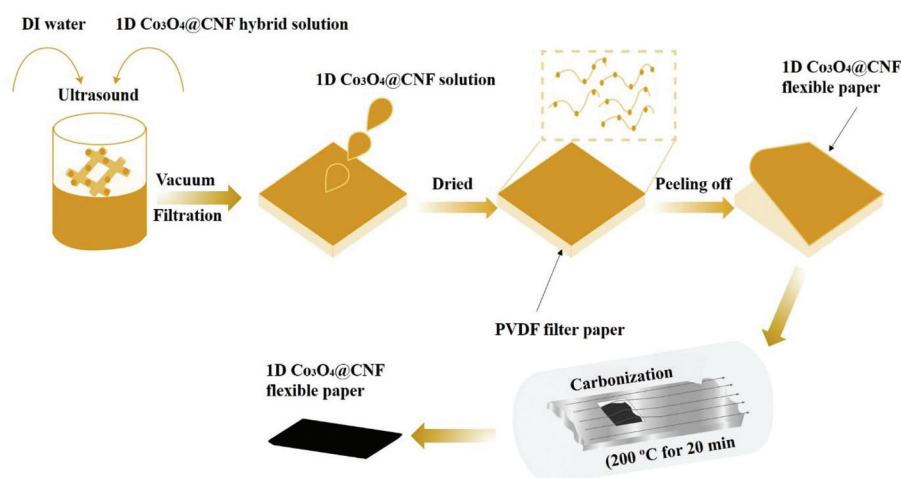
Scheme 1 Schematic vacuum filtration preparation of the 1D Co$_3$O$_4$@CNF flexible paper electrode.

3. Results and discussion

3.1. Structural properties and morphology of the 1D Co$_3$O$_4$@CNF*x* hybrid

The structure and morphology of the pristine Co$_3$O$_4$ nanoparticles and 1D Co$_3$O$_4$@CNF hybrid were analyzed by transmission electron microscopy (TEM), and energy dispersive X-ray spectroscopy (EDX) was performed to reveal the composition/percentage of each element. Fig. 1(a) and (b) represents the TEM images of the pristine Co$_3$O$_4$ nanoparticles at high and low magnifications, indicating agglomerated nanoparticles having particle sizes between 30 and 35 nm. Fig. 1(c)–(h) shows the TEM micrographs of the synthesized Co$_3$O$_4$ nanoparticles incorporating CNF with different loading amounts of Co$_3$O$_4$ precursors, which indicate that the Co$_3$O$_4$ nanoparticles are attached tightly on the surface of CNF. For instance, at a low concentration of Co$_3$O$_4$ in the 1D Co$_3$O$_4$@CNF1 (Co$_3$O$_4$: CNF = 0.5 : 1) sample, the Co$_3$O$_4$ nanoparticles were randomly attached on the rough surface of CNF, and the size of the nanoparticles was found to be 7.3 nm (Fig. 1(c) and (d)). When the concentration of Co$_3$O$_4$ increased (Co$_3$O$_4$@CNF2, Co$_3$O$_4$: CNF = 1 : 1), the Co$_3$O$_4$ nanoparticles were not only evenly dispersed on the surface of CNF but also

uniformly attached as shown in Fig. 1(e) and (f). The particle size of Co$_3$O$_4$ in Co$_3$O$_4$@CNF2 was observed to be ~5 nm. The uniform dispersion and/or tightly attached nanosized Co$_3$O$_4$ particles on the CNF surface provide them with a large surface area that is easily accessible by electrolyte *via* an inherent porous diffusion channel and robust electrical contact with the substrate, resulting in a sufficient faradaic reaction for energy storage devices.

At a higher loading of the Co$_3$O$_4$ nanoparticles (Co$_3$O$_4$: CNF = 1.5 : 1) in 1D Co$_3$O$_4$@CNF3, the CNF surface was almost wrapped by the Co$_3$O$_4$ nanoparticles with an average particle size of 12 nm as demonstrated in Fig. 1(g) and (h). Moreover, a sluggish aggregation of Co$_3$O$_4$ nanoparticles on the surface of CNF was observed (Fig. 1(h)). Fig. 1(i) shows the EDX spectra of different composites for the formation of the Co$_3$O$_4$ nanoparticles on the CNF surface. Three elements such as C, O and Co were observed from the elemental mapping of the 1D Co$_3$O$_4$@CNF hybrid (optimized ratio) as shown in S2.† The results show that the cobalt oxide nanosized particles were evenly dispersed on the surface of CNF.

The crystal structure of the prepared electrode samples has been further investigated by X-ray diffraction (XRD) analysis; the resultant diffraction pattern is illustrated in Fig. 2(a). As is
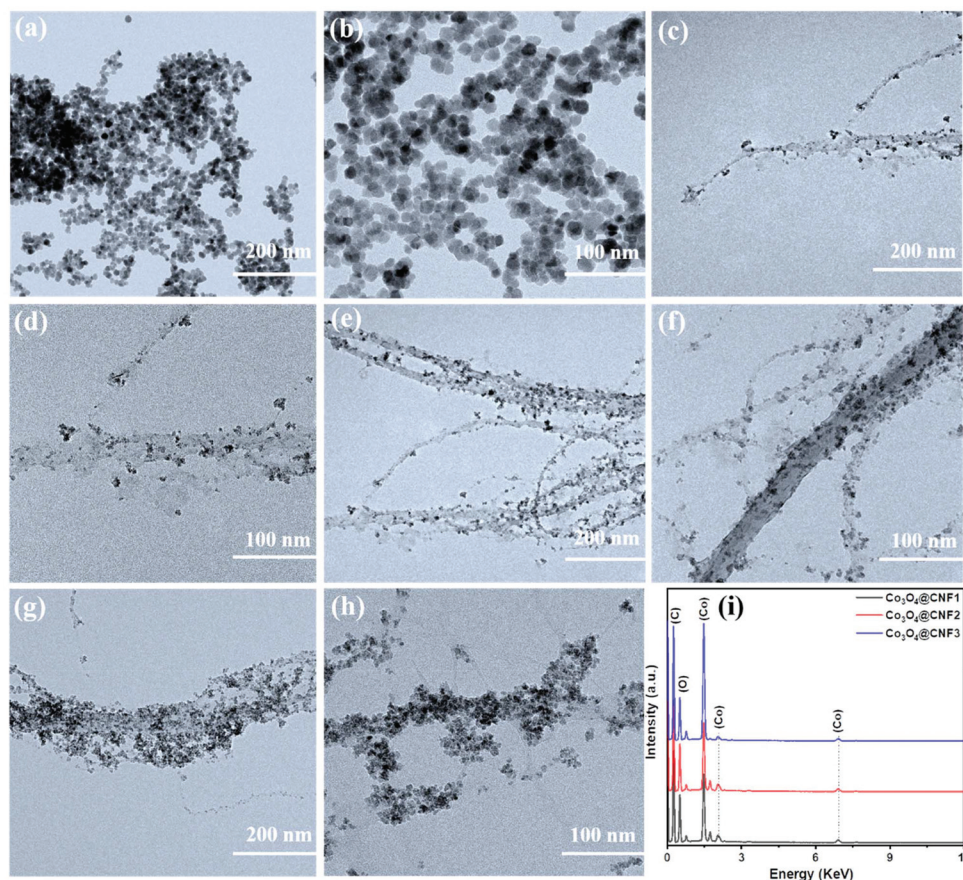

Fig. 1 TEM images at higher and lower magnification (a and b) of pristine Co$_3$O$_4$ nanoparticles, (c and d) 1D Co$_3$O$_4$@CNF1, (e and f) 1D Co$_3$O$_4$@CNF2 and (g and h) 1D Co$_3$O$_4$@CNF3 hybrid nanostructure. (i) The elemental spectra of the 1D Co$_3$O$_4$@CNF1, 1D Co$_3$O$_4$@CNF2 and 1D Co$_3$O$_4$@CNF3 hybrid nanostructure.
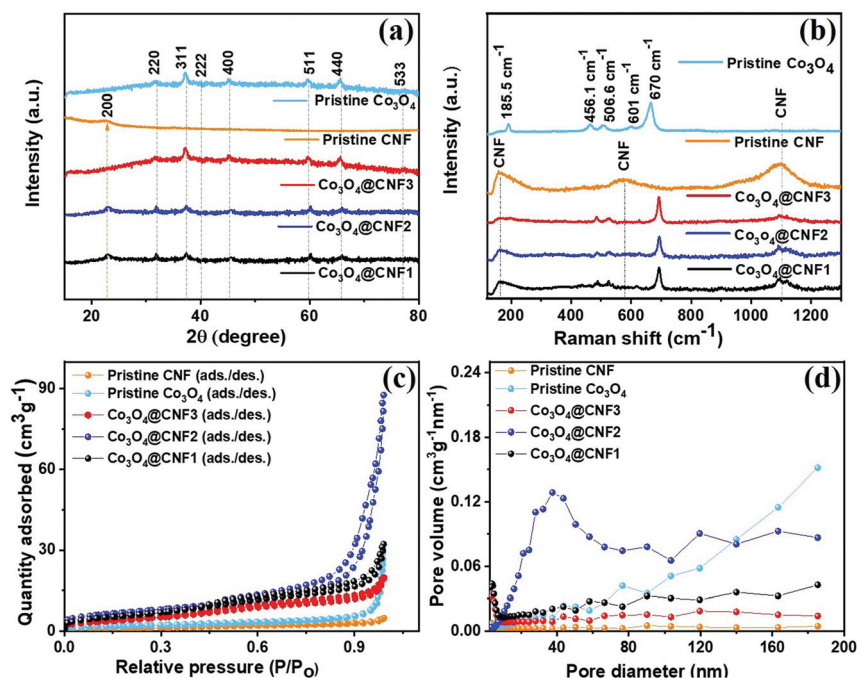
Fig. 2 (a) XRD pattern, (b) Raman spectra, (c and d) adsorption–desorption isotherm and BJH curves of the CNF, Co_3O_4 nanoparticles, 1D Co_3O_4@CNF3, 1D Co_3O_4@CNF2 and 1D Co_3O_4@CNF1 hybrids.

evident from the pattern, the diffraction peaks that appear at 31.4°, 36.8°, 39.9°, 44.9°, 59.3°, 65.3°, and 77.3° belong to (220), (311), (222), (400), (511), (440), and (533) crystallographic planes of the cubic spinal Co_3O_4 phase, revealing the formation of crystalline Co_3O_4 nanoparticles (JCPDS card no: 073-170).[42,43] The XRD pattern of CNF (CNF only) shows a single peak at $2\theta = 22.5°$, corresponding to the reflection plane of carbon (200).[44] In the case of composite electrodes, such as 1D Co_3O_4@CNF1, 1D Co_3O_4@CNF2, and 1D Co_3O_4@CNF3, characteristic peaks were observed for CNF and Co_3O_4 with a slight change in 2θ, confirming the formation of a hybrid nanostructure. As the concentration of the Co_3O_4 precursor increased from 0.5 to 1.5, the intensity of the CNF peak decreased, and the diffraction peaks of the Co_3O_4 phase were sharp, which supported the formation of a hybrid nanostructure. Furthermore, all hybrid nanostructures at different loadings of Co_3O_4 precursors that incorporated CNF also followed a similar XRD pattern. No extra peaks were observed, which was indicative of their high purity.

To further sustain the purity of Co_3O_4 nanoparticles incorporating CNF, Raman spectra were examined, as shown in Fig. 2(b). According to a previous study, Co_3O_4 with Co^{3+} ($3d^6$) and Co_2^+ ($3d^7$) existed as octahedral and tetrahedral structures, respectively.[45] It comprises the following active modes for Co_3O_4, such as "$Fd3m$" symmetry $\Gamma = E_g(R) + A_{1g}(R) + F_{1g}(IN) + 3F_{2g}(R) + 2A_{2u}(IN) + 2Eu(IN) + 2F_{2u}(IN) + 4F_{1u}(IR)$, where (R) represents the Raman active vibrations, (IR) represents the infrared active vibrations, and (IN) represents the inactive mode.[45,46]

In Fig. 2(b), the Raman spectrum of the cubic spinal Co_3O_4 nanoparticles exhibited five active Raman modes; their corresponding vibrational bands were located at ~185.8, ~456, ~506, ~601, and ~670 cm^{-1}, respectively, which is consistent with the results of XRD analysis. CNF showed three characteristic vibrational bands at 156, 670, and 1345 cm^{-1}, which could be attributed to the in-plane vibrations of sp^2 carbon-based materials with structural defects.[47] However, the 1D Co_3O_4@CNF1, 1D Co_3O_4@CNF2, and 1D Co_3O_4@CNF3 showed the characteristic vibrational bands for both Co_3O_4 nanoparticles and CNF. Furthermore, the CNF characteristic bands were weaker than those of the other two compositions, which may result from the higher loading of Co_3O_4 nanoparticle precursors. The Raman spectra for the 1D Co_3O_4@CNF2 hybrid consist of well resolved characteristic vibrational bands, highly demonstrating crystallinity.

N_2 adsorption–desorption isotherms at 77 K were used to determine the specific surface area and pore filling behaviors of the prepared composite electrodes; the results are presented in Fig. 2(c) and (d). Based on the IUPAC classifications, all electrodes exhibit the type-IV adsorption–desorption isotherm with a constant rise of 0.1–0.7 P/P_0 and negligible adsorption volume in the low gauge pressure range (Fig. 2(c)), indicating the presence of a mesoporous structure with negligible microporosity.[48] It is evident from the isotherm that the specific surface area, pore volume, and pore size distribution of all samples are dramatically different. The BET specific surface area and the BJH pore volumes were 22, 25, 16, 6, and 4 m^2g^{-1} and 0.126, 0.195, 0.167, 0.0468, and 0.0071 cm^3g^{-1} for the 1D Co_3O_4@CNF1, 1D Co_3O_4@CNF2, 1D Co_3O_4@CNF3, pristine

Co_3O_4 nanoparticles, and pristine CNF, respectively. Among them, the 1D Co_3O_4@CNF2 exhibits a relatively high specific surface area, which is three times higher than that of the pristine Co_3O_4 nanoparticles. The mesoporous structure with a high pore volume of 1D Co_3O_4@CNF$_2$ provides the necessary transport channels for electrolyte ions that could facilitate adsorption onto the electrode surface and reduce electrolyte resistance, which has a positive impact on power capability.[48] The larger specific surface area of 1D Co_3O_4@CNF2 provides an enhanced electrolyte/electrode contact area, thus facilitating the availability of more active sites for the faradaic reaction, indicating good electrochemical performance.

The synthesized bonding state and chemical composition of the 1D Co_3O_4@CNF hybrids were further confirmed by XPS spectroscopy. Fig. 3(a)–(c) shows the wide scan XPS spectra of pristine CNF, pristine Co_3O_4 nanoparticles, and the 1D Co_3O_4@CNF hybrid from 200 to 900 eV. In the case of CNF, two elements, including C 1s and O 1s corresponding to the binding energies at 286.2 eV and 532.1 eV, respectively, are

detected in the XPS wide survey scan (Fig. 3(a)). Three elements, including C 1s, O 1s, and Co 2p, were detected in Co_3O_4 nanoparticles and the 1D Co_3O_4@CNF hybrid, respectively (Fig. 3(b) and (c)). The high-resolution C 1s XPS spectrum for all samples (pristine CNF, pristine Co_3O_4, and 1D Co_3O_4@CNF) shows three peaks at 284.8 eV, 286.1 eV, and 287.8 eV which clearly indicates the presence of the C–C, C–O, and O–C–O bonds, respectively (Fig. 3(d)–(f)).[49] After the carbonization of the 1D Co_3O_4@CNF hybrid, the high resolution C 1s XPS spectrum proved that O–C–O, C–O and C–C bonds still exist in the hybridization, indicating the presence of the cellulose content in the hybridization.

Two peaks that are located at 532.8 eV in the high-resolution spectra of O 1s in CNF are attributed to the O–H and C–O–C bonds, as shown in Fig. 3(g). The high-resolution XPS spectrum of O 1s for the Co_3O_4 and 1D Co_3O_4@CNF hybrid can be deconvoluted into three components, O_{latt} (530.0 eV), O_{x^-} (531.0 eV), and $O_{adsorbates}$ (532.2 eV), as presented in Fig. 3(h) and (i). A peak at 530.0 eV was assigned to the oxygen
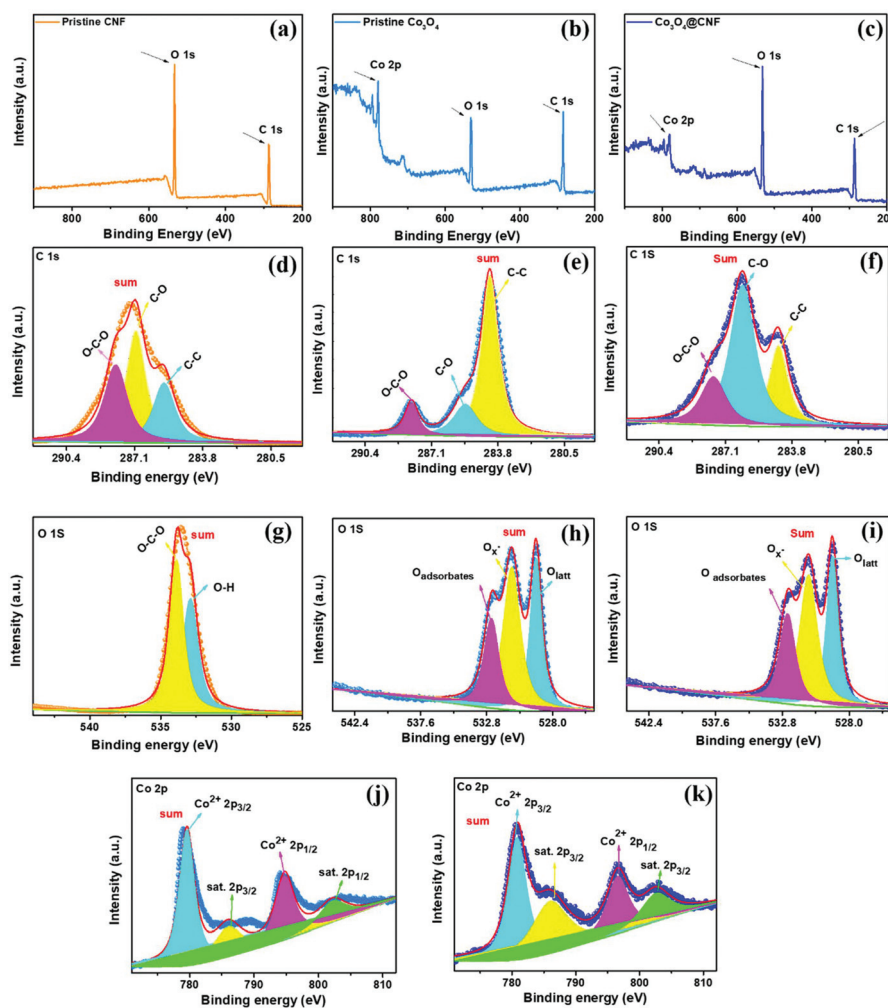

Fig. 3 (a–c) XPS survey spectra of pristine CNF, pristine Co_3O_4 nanoparticles and 1D Co_3O_4@CNF hybrid; (d–f) C 1s binding energy region, (g–i) O 1s binding energy region and (j and k) Co 2p binding energy region for the respective samples.

located in the lattice, while O_x- is ascribed to the defect oxygen or hydroxyl groups, respectively.[50] The third additional peak that appeared at 532.2 eV can be attributed to the water molecules (H–O–H), which does not always appear in the O 1s spectrum.[51,52] Moreover, the Co 2p XPS spectrum of Co_3O_4 and 1D Co_3O_4@CNF shows two distinct peaks and two weak satellite peaks, as shown in Fig. 3(j) and (k). The two-spin orbit doublets of Co_3O_4 located at 795.9 eV and 780.8 eV are attributed to Co_{2p} (1/2) and Co_{2p} (3/2), respectively, which are present in both Co_3O_4 and Co_3O_4@CNF. The presence of two satellite peaks ($Co_{ast.}$) in the vicinity of the spin orbit doublets at binding energies of 804.4 eV and 788.2 eV is in good agreement with the previous literature.[51,52] These two satellite peaks are observed for the 1D Co_3O_4@CNF hybrid, which is absent during hybridization.[53] Based on the above results, we conclude that Co_3O_4 has been successfully synthesized on the surface of CNF.

3.2. Supercapacitor performance of the 1D Co_3O_4@CNFx hybrid

Three-electrode measurement was carried out by CV, galvanostatic charging–discharging, and EIS analyses. To investigate the effect of the Co_3O_4 precursor contents on the capacitive performance of the hybrid electrode, a CV analysis was performed in a three-electrode setup in the potential range between −0.2 and 0.6 V using 3 M KOH. The CV curve of the 1D Co_3O_4@CNF hybrid electrodes with various ratios was

recorded and plotted, and the result is shown in Fig. 4(a). It was observed that all samples exhibited a typical pair of redox peaks, which were attributed to the faradaic reactions of the electrochemically active Co_3O_4 nanoparticles.[19,54,55] The different redox peak potentials are likely accredited to the diverse feeding amounts of the Co_3O_4 precursors and the size of the nanoparticles on the CNF surface. Furthermore, it is important to observe that the intensity of the redox peaks increases as the concentration of Co_3O_4 increases until the loading of Co_3O_4 over CNF reaches 1 : 1. After this point, it begins to decrease, which is attributed to the aggregation of the nanoparticles, thereby leading to a reduction in the surface area, a decrease in electrical conductivity, and as a result, a decrease in capacitance. Based on the above observations, the electrode with a loading of Co_3O_4 : CNF = 1 : 1 (1D Co_3O_4@CNF2) exhibits high current response compared to other electrodes at 20 mV s^{-1}, suggesting a higher capacitance.

CV curves of 1D Co_3O_4@CNF1 and 1D Co_3O_4@CNF3 hybrid electrodes at various scan rates (20–100 mV s^{-1}) are shown in S3(a and b),† where the current increases sharply with increasing scan rates. However, no noticeable redox peak alterations were perceived in the CV curves of 1D Co_3O_4@CNF1 and 1D Co_3O_4@CNF3 at all scan rates, suggesting a good reversibility nature.[56] To further validate the electrochemical activity in three electrode measurements, the GCD test was performed at a current density of 1 A g^{-1} in the potential window between −0.2 V and +0.6 V, as shown in Fig. 4(b). It can be seen that
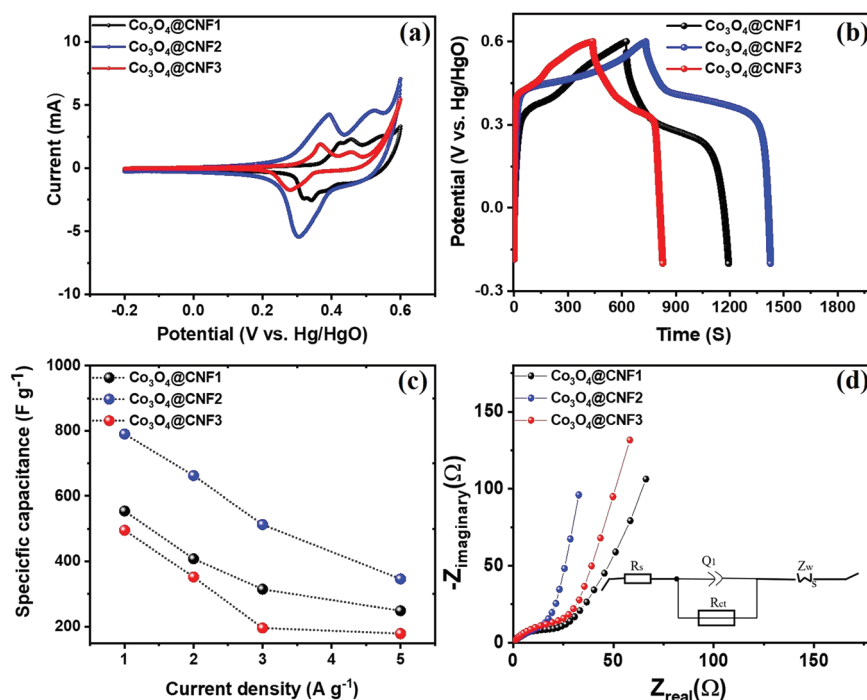

**Fig. 4** Electrochemical performance of the three-electrode measurement for the 1D Co_3O_4@CNFx hybrid electrodes (where x means the feeding amount of the Co_3O_4 nanoparticles on the CNF surface): (a) CV curve at 20 mV s^{-1} of scan rate, (b) GCD curve of 1 A g^{-1} of current density, (c) specific capacitance at the various current densities and (d) electrochemical impedance spectra (EIS).

the discharge curve with respect to the time dependence of potential is nonlinear, which is a typical characteristic of pseudocapacitance.[57] The GCD curves were collected at various current densities of 1, 2, 3, and 5 A g^{-1} for 1D Co$_3$O$_4$@CNF1 and 1D Co$_3$O$_4$@CNF3; the results are shown in S4(a and b).† At low current density, the charging curves of all samples exhibit sluggish behavior because of the diffusion-controlled faradaic process together with purely capacitive charging.[58] The discharge times of these hybrid electrodes are found in the order of Co$_3$O$_4$@CNF2 > Co$_3$O$_4$@CNF1 > Co$_3$O$_4$@CNF3 at a current density of 1 A g^{-1}. The C_s values of the 1D Co$_3$O$_4$@CNF1, Co$_3$O$_4$@CNF2, and Co$_3$O$_4$@CNF3 hybrid electrodes are observed to be 554.7, 408.0, 314.7, and 248.56 F g^{-1}; 789.9, 662.6, 513.16, and 346.3 F g^{-1}; and 495.6, 352.3, 195.7, and 178.7 F g^{-1} at current densities of 1, 2, 3, and 5 A g^{-1}, respectively, as presented in Fig. 4(c). Furthermore, the electrochemical kinetics of the 1D Co$_3$O$_4$@CNFx hybrid electrode was investigated through AC impedance analysis (Fig. 4(d)). The equivalent circuits of the hybrid electrodes are presented in the inset of Fig. 4(d), wherein, R_s is the internal series resistance, R_{ct} is the charge-transfer resistance, Q_1 is the constant phase element, and W_z is the Warburg impedance. The equivalent series resistance (R_s) of the Co$_3$O$_4$@CNF2 hybrid electrode (~0.152 Ω) is lower than that of the Co$_3$O$_4$@CNF1 (~0.352 Ω) and Co$_3$O$_4$@CNF3 (~0.245 Ω) hybrid electrodes. These results suggest that the 1D Co$_3$O$_4$@CNF2 hybrid electrode has a higher conductivity, obtained from the linear extrapolation of the low-frequency region of the Nyquist plot with the real axis. The charge transfer resistance (R_{ct}) of the 1D Co$_3$O$_4$@CNF2 hybrid electrode is estimated to be ~11.86 Ω, lower than that of Co$_3$O$_4$@CNF1 (~17.9 Ω) and Co$_3$O$_4$@CNF3 (~21.23 Ω) hybrid electrodes, indicating a rapid redox kinetics in the 1D Co$_3$O$_4$@CNF2 hybrid electrode, and consistent with the CV and GCD results.

3.3. Comparative supercapacitor performance of pristine Co$_3$O$_4$, pristine CNF, and 1D Co$_3$O$_4$@CNF hybrid electrodes

To compare the electrochemical performance of the hybrid electrodes, CV, GCD, and EIS analyses were performed in 3 M KOH aqueous electrolyte using three electrode measurements within a potential window of −0.2 V to +0.6 V (*vs.* Hg/HgO). Fig. 5(a) and (b) depicts the comparative CV and GCD curves of the Ni foam, pristine Co$_3$O$_4$, pristine CNF, and 1D Co$_3$O$_4$@CNF hybrid electrode at a scan rate of 20 mV s^{-1} and a current density of 1 A g^{-1}. The results clearly demonstrate that the CV integrated area and the GCD longest discharge time of the 1D Co$_3$O$_4$@CNF hybrid electrode exhibit the highest capacitance among the electrodes tested. In contrast, the current response of the Ni foam is negligible compared to that of the other electrodes, revealing that there is no capacitance contribution of the current collector. As anticipated, two peaks are present in the anodic and cathodic sweeps of the CV curves for pristine Co$_3$O$_4$ and 1D Co$_3$O$_4$@CNF hybrid electrodes; these peaks are associated with the reversible redox

couples of Co^{2+}/Co^{3+} and Co^{3+}/Co^{4+} in the alkaline electrolyte, as presented in following equations.[19]

$$Co_3O_4 + H_2O + OH^- \leftrightarrow 3CoOOH + e^- \qquad (6)$$

$$CoOOH + OH^- \leftrightarrow CoO_2 + H_2O + e^- \qquad (7)$$
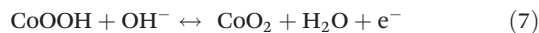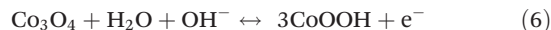
When the scan rates and current densities increase, the shapes of the CV and GCD curves are well maintained due to the presence of more prominent redox peaks, as shown in Fig. 5(c) and (d). This observation demonstrates the high reversibility and excellent rate capability of the 1D Co$_3$O$_4$@CNF hybrid electrode (80% capacitance retention at four-times higher current density). CV and GCD curves for pristine Co$_3$O$_4$ and pristine CNF at diverse scan rates and current densities, respectively, are shown in S5(a, b) and S6(a, b).† Based on these results, the 1D Co$_3$O$_4$@CNF hybrid electrode delivered a C_s value of 789.9 F g^{-1} at a current density of 1 A g^{-1}, which is the highest among published reports (Table S1†).

To further investigate the capacitive properties and electron/ion transfer behavior of the electrodes, EIS measurement was employed, and the resultant plot is presented in Fig. 5(f). The semicircle part in the high frequency region is associated with charge transfer resistance (R_{ct}) at the interface between the electrolyte and/or electrode surface (semicircle diameter appearing from the oxidation state of the Co$_2{}^+$/Co^{3+} and reversible redox couples Co^{3+}/Co^{4+}). Notably, the 1D Co$_3$O$_4$@CNF hybrid electrode shows a lower R_{ct} value of ~11.86 Ω compared to pristine Co$_3$O$_4$ (~16.1Ω) and pristine CNF (~41.6 Ω), which further substantiates its good conductivity and galloping electron transfer kinetics. More importantly, our 1D Co$_3$O$_4$@CNF hybrid electrode shows a much higher capacitive contribution among the three electrodes' electrochemical performance.

3.4. Symmetric supercapacitor performance of the 1D Co$_3$O$_4$@CNF hybrid electrode

It has been proven that a wide potential window is one of the important key parameters for enhancing the energy density of high performance SCs. To evaluate the SSC performance for practical applications, both positive and negative electrodes were prepared using 1D Co$_3$O$_4$@CNF electrodes, as presented in the schematic illustration in Fig. 6(a).

CV and GCD curves of the 1D Co$_3$O$_4$@CNF hybrid SSC device at various voltage windows are shown in Fig. 6(b) and (c). In this study, the stable working potential of the 1D Co$_3$O$_4$@CNF hybrid SSC electrode was observed to be 0 to 1 V because of the limitations arising from oxygen evolution at potentials higher than 1 V. Therefore, the potential range up to 1 V was selected in 3 M KOH aqueous electrolyte for electrochemical performances of the as assembled SSC device. Fig. 6(d) shows the CV curves of Ni foam, pristine CNF, pristine Co$_3$O$_4$, and 1D Co$_3$O$_4$@CNF hybrid electrodes at a scan rate of 20 mV s^{-1}. Remarkably, the current generated by the 1D Co$_3$O$_4$@CNF based electrode is much larger than that of pristine CNF and pristine Co$_3$O$_4$ nanoparticle electrodes. The pristine Co$_3$O$_4$ nanoparticles and 1D Co$_3$O$_4$@CNF hybrid electrode exhibit a pair of distinct oxidation and reduction peaks at
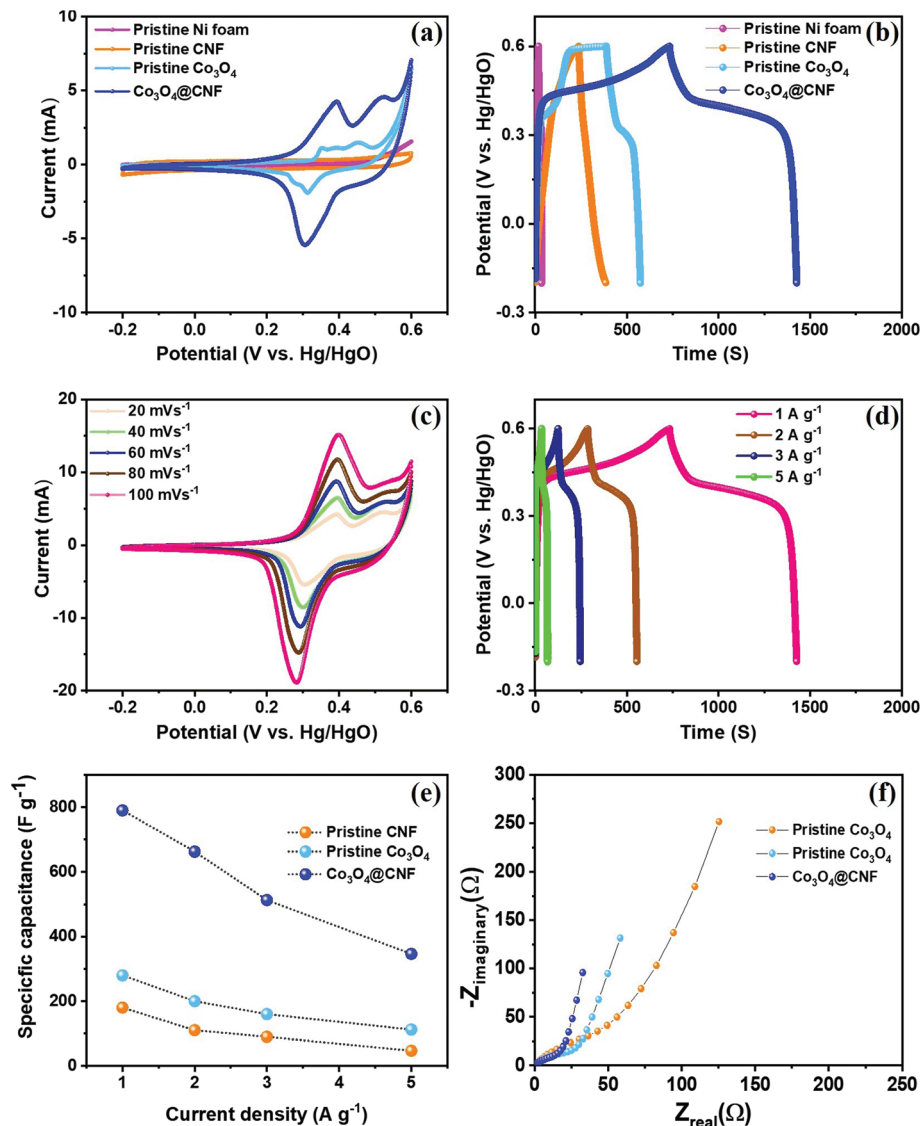
Fig. 5 Comparison of three electrode electrochemical measurements for the pristine Co_3O_4 nanoparticles, pristine CNF and 1D Co_3O_4@CNF: (a) CV curve at 20 mV s^{-1} of scan rate, (b) GCD curve of 1 A g^{-1} of current density, (c and d) CV and GCD curves at various scan rates and current densities, (e) specific capacitance and (f) EIS measurement.

20 mV s^{-1}, which is indicative of a reversible electrochemical reaction. The 1D Co_3O_4@CNF based electrode shows both the largest current response and integral CV area, revealing the highest capacitance (Fig. 6d). The CV profiles of the synthesized 1D Co_3O_4@CNF based electrode at various scan rates are shown in Fig. 6(e), where the current response was enhanced sharply with increasing scan rates. However, the increasing scan rates do not influence the shape of the CV profiles significantly, even at higher scan rates, such as 100 mV s^{-1}, suggesting a good reversibility/electron conduction nature of the 1D Co_3O_4@CNF hybrid SSC electrode.[41,59] The CV curves of the pristine Co_3O_4 nanoparticle and pristine CNF electrodes at various scan rates are shown in S7(a) and (b).† A higher scan rate constrained the electrolyte ions in accessing the full surface of the samples by reducing the diffusion time,

leading to decreased capacitance.[60] The consistency of the CV curves using multiple cycles is an imperative factor in identifying electrode characteristics. Hence, various random cycles were performed for the 1D Co_3O_4@CNF hybrid at 20 mV s^{-1}, which shows highly overlapped CV curves for sustained performance (Fig. 6(f)).

GCD was tested at different current densities with the same potential to further demonstrate the capacitive output of the 1D Co_3O_4@CNF. Fig. 6(g) shows the comparative GCD curves for pristine CNF, pristine Co_3O_4 nanoparticles, and 1D Co_3O_4@CNF hybrid electrodes at a current density of 1 A g^{-1}. Among these samples, the 1D Co_3O_4@CNF hybrid electrode has the longest discharge time with nonstandard triangular shape obtained from the GCD curve and in accordance with the CV curve. Moreover, the GCD curve at different current
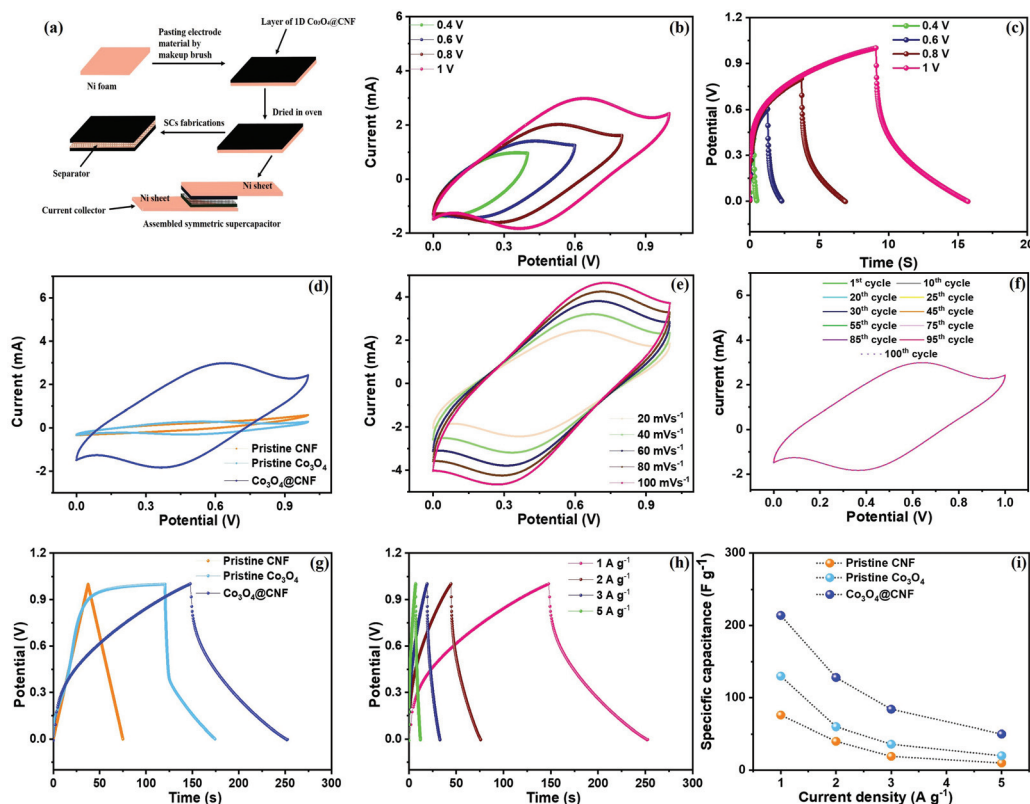
Fig. 6 Electrochemical performance of the SSC on the pristine Co$_3$O$_4$ nanoparticles, pristine CNF and 1D Co$_3$O$_4$@CNF hybrid electrodes: (a) simplistic schematic illustration of the SSC device that consisted of similar two 1D Co$_3$O$_4$@CNF hybrid electrodes, (b and c) CV and GCD curves collected at various voltage windows, (d) comparison CV curve at 20 mV s^{-1}, (e) CV curve at, (f) cycling CV curves over 100 cycles, (g and h) comparison GCD curve at 1 A g^{-1} and at various current densities, respectively, (i) specific capacitance at different current densities.

densities was obtained for the 1D Co$_3$O$_4$@CNF hybrid electrode and is illustrated in Fig. 6(h). Likewise, GCD curves for the pristine Co$_3$O$_4$ nanoparticle and pristine CNF electrodes were recorded at different current densities and are shown in S8(a) and (b).†

The C_s value of the 1D Co$_3$O$_4$@CNF hybrid electrode exhibits a higher capacitance of 214 F g^{-1} compared to that of the pristine Co$_3$O$_4$ nanoparticles (~130 F g^{-1}) and CNF (~76 F g^{-1}) at a current density of 1 A g^{-1}, which is calculated using eqn (3) presented in Fig. 6(i). However, the value of C_s achieved for the 1D Co$_3$O$_4$@CNF hybrid electrode is higher than that previously reported for TMOs and their mixed hybrids incorporated with carbon-based materials and conductive polymers (Table S2†).

Fig. 7(a) shows the EIS plot of the 1D Co$_3$O$_4$@CNF hybrid SSC electrode, demonstrating a lower R_{ct} value of ~0.713 Ω compared to that of pristine Co$_3$O$_4$ (~4.9 Ω) and pristine CNF (~2.54 Ω). The low R_{ct} value of the 1D Co$_3$O$_4$@CNF hybrid SSC electrode indicates the low internal diffusion resistance, fast ion/electron transfer kinetics, and good capacitive performance of the SSC device. The long-term cyclic performance of the 1D Co$_3$O$_4$@CNF hybrid SSC electrode was further determined through GCD analysis at a constant current rate of 10 A g^{-1}, as shown in Fig. 7(b). The 1D Co$_3$O$_4$@CNF hybrid SSC

device retains 94% of the initial capacitance after 5000 GCD cycles, higher than those for pristine Co$_3$O$_4$ (79%) and pristine CNF (89%). The coulombic efficiency (%) was determined using eqn (7) and the results are shown in Fig. 7(c). The coulombic efficiency of 1D Co$_3$O$_4$@CNF stabilizes at nearly 98%, 96% for the pristine CNF and 92% for the pristine Co$_3$O$_4$, demonstrating a good cycling performance of the hybrid SSC device. This can be ascribed to the superior structural stability of the 1D Co$_3$O$_4$@CNF hybrid SSC device, resulting from tightly attached Co$_3$O$_4$ nanoparticles on the CNF surface (hydrophilic CNF was used as the backbone of Co$_3$O$_4$). Fig. 7(d) shows the Ragone plot of the 1D Co$_3$O$_4$@CNF hybrid SSC device. At various current densities, the energy density (E) against power density (P) plots for the pristine Co$_3$O$_4$, pristine CNF and 1D Co$_3$O$_4$@CNF are shown in S9.† From all the above results, the 1D Co$_3$O$_4$@CNF hybrid SSC device provided a maximum energy density of 26.7 W h kg^{-1} at a power density up to 0.9 kW kg^{-1}, which is higher than that of previously published reports.[61–68] Based on the results, the 1D Co$_3$O$_4$@CNF and particularly pristine Co$_3$O$_4$ exhibits the nonlinear discharging curve. Thus, energy density (E) and power density (P) were further calculated using the nonlinear GCD curve following the previous published reports (S10†),[69,70] and the results are illustrated in S11.† The 1D Co$_3$O$_4$@CNF hybrid SSC electrode
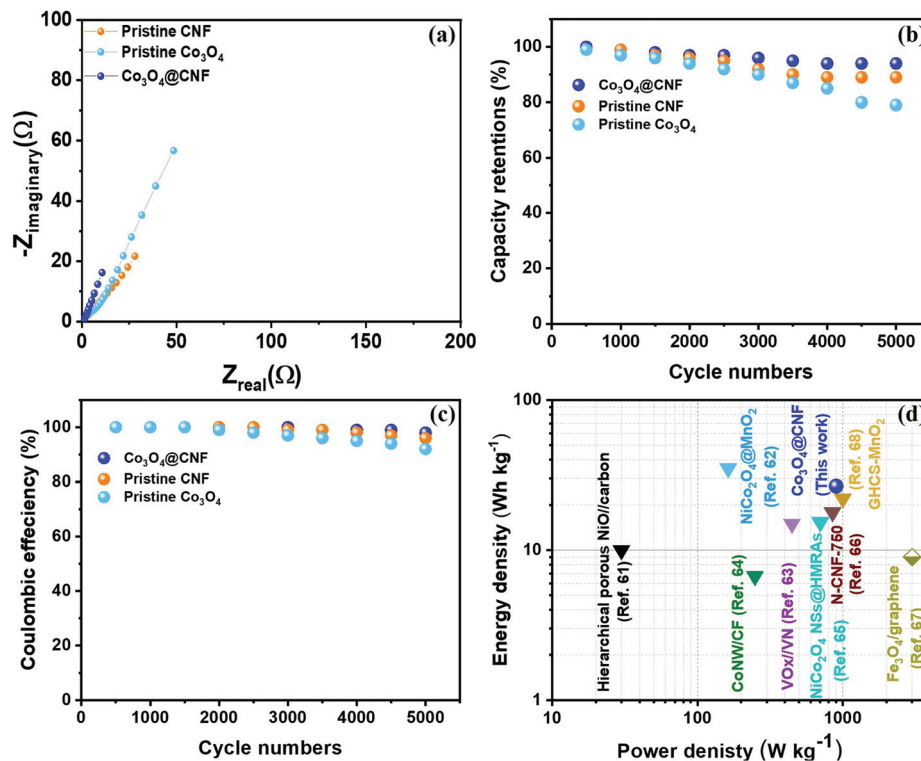
Fig. 7 Electrochemical performance of the SSC devices for the pristine Co_3O_4 nanoparticles, pristine CNF and 1D Co_3O_4@CNF hybrid electrodes: (a) EIS plot, (b and c) capacity of retentions and coulombic efficiency of electrodes at 15 A g^{-1} of current density over 5000 cycles and (d) Ragone plot.

delivers a maximum energy density of 8.7 W h kg^{-1} when the power density was 306 W kg^{-1} at a current density of 1 A g^{-1}, which is higher than that of the pristine Co_3O_4 such as 3.03 W h kg^{-1} at a power density of 203.1 W kg^{-1}.

3.5. Flexible symmetric supercapacitor performance of the 1D Co_3O_4@CNF hybrid electrode

The morphology of the 1D Co_3O_4@CNF hybrid paper-like film was investigated by FESEM, and the results are shown in S12(a) and (b).† The FESEM micrographs show that the Co_3O_4 nanoparticles were still attached on the surface of the CNF. The chemical composition of the 1D Co_3O_4@CNF hybrid paper-like film was then examined by EDX spectroscopy, as can be seen in S13.† The EDX spectrum shows that the three elements such as C, O and Co with the atomic % ratio of 55.58, 32.37 and 12.05%, respectively. The morphology analysis indicates that the Co_3O_4 nanoparticles were tightly attached on the surface of the CNF as the hybrid. Then, the 1D Co_3O_4@CNF hybrid paper-like film was used to fabricate the flexible SSC without any current collectors, binders, and additives. The paper-like film was annealed at 200 °C for 20 min in a mixture of H_2/Ar atmosphere to improve the intrinsic conductivity (Scheme 1). The digital images of the 1D Co_3O_4@CNF flexible SSC device at different positions are presented in Fig. 8(a). The PVA–KOH gel was preferred as the electrolyte, and the cellulose separator (15 μm thick, Dream waver)

was soaked for a few minutes and then sandwiched between the two flexible identical electrodes with silver wires (Fig. 8(b)). The CV curves for the 1D Co_3O_4@CNF hybrid flexible paper show various voltage windows ranging from 0–0.8 V to 0–1 V; the selected stable voltage window was 1 V (Fig. 8(c)). At several scan rates (20–100 mV s^{-1}), the CV curve sustains its shape even at high scan rates, indicating the good stability of the 1D Co_3O_4@CNF flexible electrode (Fig. 8(d)). The CV curves of 1D Co_3O_4@CNF flexible paper in normal and bend states at different angles are shown in Fig. 8(e). It shows that the bending degree of the 1D Co_3O_4@CNF flexible electrode has no effect on the electrochemical performance, and the integrated area of the CV curve remains the same as that of the normal CV. More importantly, the shape of the CV curve of 1D Co_3O_4@CNF flexible paper does not change obviously after various random bending cycles at 20 mV s^{-1} (S14†), demonstrating that the SCs performance is unaffected by bending cycles (because of good CNF flexibility). The GCD curves of the 1D Co_3O_4@CNF flexible paper at various current densities are shown in Fig. 8(f). The C_s values calculated from the discharge curves are shown in Fig. 8(g). The 1D Co_3O_4@CNF flexible paper has a C_s value of 80 F g^{-1} at a current density of 1 A g^{-1}. Compared with the SCs performance (47 F cm^{-3} at 0.9 A cm^{-3}) reported by kuzmenko, the energy density of the CNF/rGO composite electrode was about 1.46 W h L^{-1} at a power density of 1.09 kW L^{-1}. The SCs performance of the CNF/rGO compo-
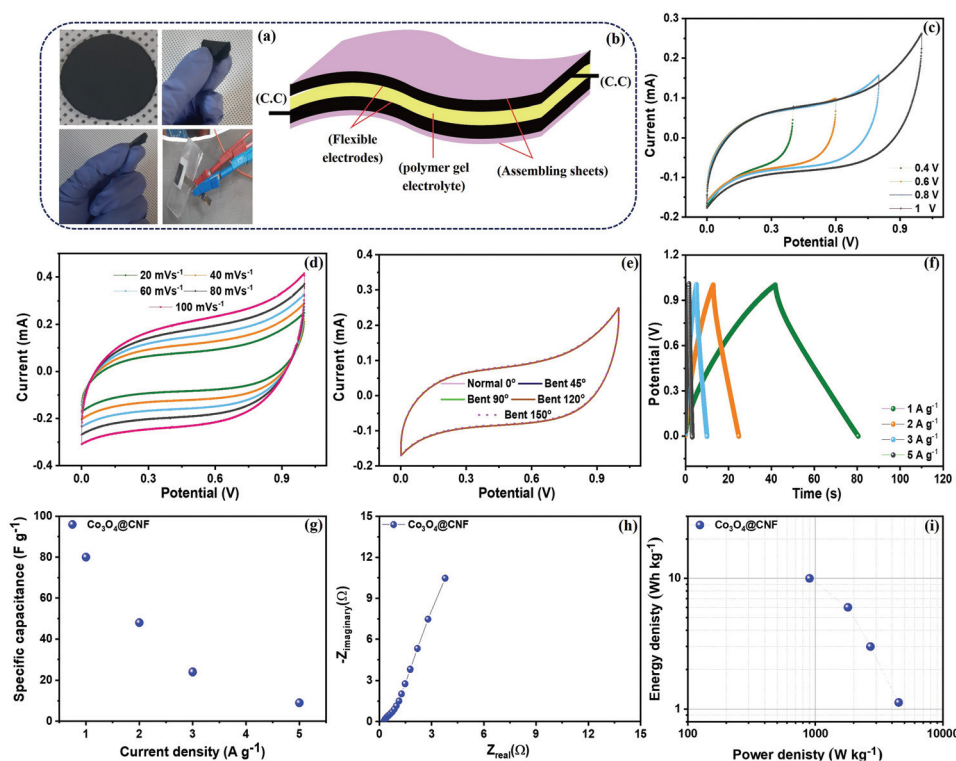
Fig. 8 Electrochemical performance of the flexible SSC in the voltage window from 0 V to 1 V using the PVA–KOH polymer gel electrolyte for 1D Co_3O_4@CNF flexible paper: (a) digital photo images of the 1D Co_3O_4@CNF hybrid flexible electrode at different positions, (b) illustration of the assembled form of the flexible SSCs, (c) CV curves at the various voltage windows, (d) CV curve at the various scan rates, (e) CV curve at 20 mV s^{-1} under normal and bending states at diverse angles, (f) GCD curves at various current densities, (g) specific capacitance, (h) EIS plot and (i) Ragone plot.

site electrode is observed to be significantly lower.[71] Our result demonstrated that the 1D Co_3O_4@CNF flexible paper has an excellent capacitive performance as well as maintains the flexibility even after carbonization and rapid current voltage response.

EIS is a significant method for an in-depth study of the capacitive performance of flexible SSC. Fig. 8(h) shows the Nyquist plots of the 1D Co_3O_4@CNF flexible paper. The Nyquist plot of the 1D Co_3O_4@CNF flexible paper is nearly vertical, indicating ideal capacitive behavior. A small R_{ct} value of ~0.537 Ω is observed in the 1D Co_3O_4@CNF flexible paper, suggesting high electronic mobility and good capacitive properties because of the gel electrolyte. The energy density (E) and power density (P) are vital parameters of electrochemical measurements used for commercial scale applications. The assessed energy density values are 10, 6, 3, and 1.12 W h kg^{-1} for the 1D Co_3O_4@CNF hybrid electrode at 0.9, 1.8, 2.7, and 4.5 K W kg^{-1}, respectively, as shown in Fig. 8(i). The 1D Co_3O_4@CNF hybrid electrode demonstrates an energy density as high as 10 W h kg^{-1} with a corresponding power density of 0.9 kW kg^{-1} when the current density reaches 1 A g^{-1}, revealing a higher performance of energy and power density among several other published flexible symmetric electrodes.[37,72–75] Such a cost effective, eco-friendly flexible electrode exhibits a

higher electrochemical performance, which can open a new avenue in the field of flexible electronics.

4. Conclusions

In summary, a simple, cost effective, and well-designed synthetic sol–gel route was employed to synthesize a 1D Co_3O_4@CNF hybrid electrode. Specifically, the Co_3O_4 precursor ratio was noted to be a critical factor that affected the formation (i.e., dispersion stability, surface area, and improved conductivity) of the 1D Co_3O_4@CNF hybrid nanostructure and further influenced the distinct electrode activity for the SCs. This hybrid electrode showed the highest C_s value of ~214 F g^{-1} with a remarkable capacity retention of ~94% even after 5000 cycles. Nonetheless, such high performance of the 1D Co_3O_4@CNF hybrid electrode can be attributed to the well-attached nanosized Co_3O_4 particles on the 1D CNF surface that provide a large surface area for the fast faradaic and non-faradaic processes. Remarkably, 1D hydrophilic CNF incorporated Co_3O_4 could improve ion diffusion and prevent structural collapse in the GCD process, while the 1D nanostructure promoted charge transfer, further boosting the performance of the 1D Co_3O_4@CNF electrode. Therefore, binder free

nature of the 1D Co_3O_4@CNF, the highly conductive 1D hybrid nanostructure (carbonized at 200 °C for about 20 min under a H_2/Ar atmosphere), enabled it to serve as a powerful platform for fabricating a flexible paper-like electrode with outstanding capacitive performance, including C_s (~80 F g^{-1}) and a superior energy density of 10 W h kg^{-1} at a power density of 0.9 kW kg^{-1}. These findings provide new insight into designing flexible/wearable SSC for higher capacitive performance.

Conflicts of interest

There are no conflicts to declare.

Acknowledgements

References

1 M. F. El-Kady, V. Strong, S. Dubin and R. B. Kaner, Laser scribing of high-performance and flexible graphene-based electrochemical capacitors, *Science*, 2012, **335**, 1326–1330.

2 T. Cheng, Y. Zhang, W. Y. Lai and W. Huang, Stretchable thin–film electrodes for flexible electronics with high deformability and stretchability, *Adv. Mater.*, 2015, **27**, 3349–3376.

3 Y. Zhang, Y. Huang and J. A. Rogers, Mechanics of stretchable batteries and supercapacitors, *Curr. Opin. Solid State Mater. Sci.*, 2015, **19**, 190–199.

4 C. Shao, T. Xu, J. Gao, Y. Liang, Y. Zhao and L. Qu, Flexible and integrated supercapacitor with tunable energy storage, *Nanoscale*, 2017, **9**, 12324–12329.

5 X. Zang, X. Li, M. Zhu, X. Li, Z. Zhen, Y. He, K. Wang, J. Wei, F. Kang and H. Zhu, Graphene/polyaniline woven fabric composite films as flexible supercapacitor electrodes, *Nanoscale*, 2015, **7**, 7318–7322.

6 G. Wang, L. Zhang and J. Zhang, A review of electrode materials for electrochemical supercapacitors, *Chem. Soc. Rev.*, 2012, **41**, 797–828.

7 S. G. Mohamed, I. Hussain and J.-J. Shim, One-step synthesis of hollow C-$NiCo_2S_4$ nanostructures for high-performance supercapacitor electrodes, *Nanoscale*, 2018, **10**, 6620–6628.

8 C. Ren, X. Jia, W. Zhang, D. Hou, Z. Xia, D. Huang, J. Hu, S. Chen and S. Gao, Hierarchical Porous Integrated $Co1–xS$/$CoFe_2O_4$@rGO Nanoflowers Fabricated via Temperature–Controlled In Situ Calcining Sulfurization of

Multivariate CoFe–MOF–74@rGO for High–Performance Supercapacitor, *Adv. Funct. Mater.*, 2020, 2004519.

9 J. Cherusseri, D. Pandey, K. S. Kumar, J. Thomas and L. Zhai, Flexible supercapacitor electrodes using metal–organic frameworks, *Nanoscale*, 2020, **12**, 17649–17662.

10 I. Rabani, R. Zafar, K. Subalakshmi, H.-S. Kim, C. Bathula and Y.-S. Seo, A facile mechanochemical preparation of Co_3O_4@ g-C_3N_4 for application in supercapacitors and degradation of pollutants in water, *J. Hazard. Mater.*, 2020, 124360.

11 X. Wu, Z. Han, X. Zheng, S. Yao, X. Yang and T. Zhai, Core-shell structured Co_3O_4@ $NiCo_2O_4$ electrodes grown on flexible carbon fibers with superior electrochemical properties, *Nano Energy*, 2017, **31**, 410–417.

12 N. Jabeen, A. Hussain, Q. Xia, S. Sun, J. Zhu and H. Xia, High–performance 2.6 V aqueous asymmetric supercapacitors based on in situ formed Na0. 5MnO_2 nanosheet assembled nanowall arrays, *Adv. Mater.*, 2017, **29**, 1700804.

13 J. Li, W. Zhao, F. Huang, A. Manivannan and N. Wu, Single-crystalline $Ni(OH)_2$ and NiO nanoplatelet arrays as supercapacitor electrodes, *Nanoscale*, 2011, **3**, 5103–5109.

14 E. Samuel, B. Joshi, M.-W. Kim, Y.-I. Kim, M. T. Swihart and S. S. Yoon, Hierarchical zeolitic imidazolate framework-derived manganese-doped zinc oxide decorated carbon nanofiber electrodes for high performance flexible supercapacitors, *Chem. Eng. J.*, 2019, **371**, 657–665.

15 G. Zhu, Z. He, J. Chen, J. Zhao, X. Feng, Y. Ma, Q. Fan, L. Wang and W. Huang, Highly conductive three-dimensional MnO_2–carbon nanotube–graphene–Ni hybrid foam as a binder-free supercapacitor electrode, *Nanoscale*, 2014, **6**, 1079–1085.

16 X. Liu, G. Sheng, M. Zhong and X. Zhou, Hybrid nanowires and nanoparticles of WO_3 in a carbon aerogel for supercapacitor applications, *Nanoscale*, 2018, **10**, 4209–4217.

17 Z. S. Wu, D. W. Wang, W. Ren, J. Zhao, G. Zhou, F. Li and H. M. Cheng, Anchoring hydrous RuO_2 on graphene sheets for high–performance electrochemical capacitors, *Adv. Funct. Mater.*, 2010, **20**, 3595–3602.

18 L. Xing, Y. Dong and X. Wu, Hierarchical Co_3O_4@Co_9S_8 nanowall structures assembled by many nanosheets for high performance asymmetric supercapacitors, *RSC Adv.*, 2018, **8**, 28172–28178.

19 Q. Liao, N. Li, S. Jin, G. Yang and C. Wang, All-solid-state symmetric supercapacitor based on Co_3O_4 nanoparticles on vertically aligned graphene, *ACS Nano*, 2015, **9**, 5310–5317.

20 H. Wang, J. Guo, C. Qing, D. Sun, B. Wang and Y. Tang, Novel topotactically transformed carbon–CoO–NiO–$NiCo_2O_4$ nanosheet hybrid hetero-structured arrays as ultrahigh performance supercapacitors, *Chem. Commun.*, 2014, **50**, 8697–8700.

21 Y. Huang, H. Li, M.-S. Balogun, W. Liu, Y. Tong, X. Lu and H. Ji, Oxygen vacancy induced bismuth oxyiodide with remarkably increased visible-light absorption and superior

photocatalytic performance, *ACS Appl. Mater. Interfaces*, 2014, **6**, 22920–22927.

22 L. L. Zhang and X. Zhao, Carbon-based materials as supercapacitor electrodes, *Chem. Soc. Rev.*, 2009, **38**, 2520–2531.

23 H. Tabuchi, K. Urita and I. Moriguchi, Effect of Carbon Nanospace on Charge–Discharge Properties of Si and SiO x Nanoparticles-Embedded Nanoporous Carbons, *Bull. Chem. Soc. Jpn.*, 2015, **88**, 1378–1384.

24 J. Yan, T. Wei, W. Qiao, B. Shao, Q. Zhao, L. Zhang and Z. Fan, Rapid microwave-assisted synthesis of graphene nanosheet/Co3O4 composite for supercapacitors, *Electrochim. Acta*, 2010, **55**, 6973–6978.

25 Y. Xiao, S. Liu, F. Li, A. Zhang, J. Zhao, S. Fang and D. Jia, 3D hierarchical Co_3O_4 twin–spheres with an urchin–like structure: Large–scale synthesis, multistep–splitting growth, and electrochemical pseudocapacitors, *Adv. Funct. Mater.*, 2012, **22**, 4052–4059.

26 J. Zhang, J. Lin, J. Wu, R. Xu, M. Lai, C. Gong, X. Chen and P. Zhou, Excellent electrochemical performance hierarchical $Co_3O_4@Ni_3S_2$ core/shell nanowire arrays for asymmetric supercapacitors, *Electrochim. Acta*, 2016, **207**, 87–96.

27 S. Xiong, C. Yuan, X. Zhang, B. Xi and Y. Qian, Controllable synthesis of mesoporous Co_3O_4 nanostructures with tunable morphology for application in supercapacitors, *Chem. – Eur. J.*, 2009, **15**, 5320–5326.

28 X. Zhou, Q. Chen, A. Wang, J. Xu, S. Wu and J. Shen, Bamboo-like composites of V_2O_5/polyindole and activated carbon cloth as electrodes for all-solid-state flexible asymmetric supercapacitors, *ACS Appl. Mater. Interfaces*, 2016, **8**, 3776–3783.

29 C. Yuan, L. Yang, L. Hou, L. Shen, X. Zhang and X. W. D. Lou, Growth of ultrathin mesoporous Co_3O_4 nanosheet arrays on Ni foam for high-performance electrochemical capacitors, *Energy Environ. Sci.*, 2012, **5**, 7883–7887.

30 X.-H. Xia, J.-P. Tu, Y.-J. Mai, X.-L. Wang, C.-D. Gu and X.-B. Zhao, Self-supported hydrothermal synthesized hollow Co_3O_4 nanowire arrays with high supercapacitor capacitance, *J. Mater. Chem.*, 2011, **21**, 9319–9325.

31 D. W. Wang, H. T. Fang, F. Li, Z. G. Chen, Q. S. Zhong, G. Q. Lu and H. M. Cheng, Aligned titania nanotubes as an intercalation anode material for hybrid electrochemical energy storage, *Adv. Funct. Mater.*, 2008, **18**, 3787–3793.

32 F. Grote, R.-S. Kühnel, A. Balducci and Y. Lei, Template assisted fabrication of free-standing MnO_2 nanotube and nanowire arrays and their application in supercapacitors, *Appl. Phys. Lett.*, 2014, **104**, 053904.

33 Y. Fu, H. Wu, S. Ye, X. Cai, X. Yu, S. Hou, H. Kafafy and D. Zou, Integrated power fiber for energy conversion and storage, *Energy Environ. Sci.*, 2013, **6**, 805–812.

34 L. Nyholm, G. Nyström, A. Mihranyan and M. Strømme, Toward flexible polymer and paper–based energy storage devices, *Adv. Mater.*, 2011, **23**, 3751–3769.

35 D. P. Dubal, J. G. Kim, Y. Kim, R. Holze, C. D. Lokhande and W. B. Kim, Supercapacitors based on flexible substrates: an overview, *Energy Technol.*, 2014, **2**, 325–341.

36 X. Lu, M. Yu, G. Wang, Y. Tong and Y. Li, Flexible solid-state supercapacitors: design, fabrication and applications, *Energy Environ. Sci.*, 2014, **7**, 2160–2181.

37 K. Gao, Z. Shao, J. Li, X. Wang, X. Peng, W. Wang and F. Wang, Cellulose nanofiber–graphene all solid-state flexible supercapacitors, *J. Mater. Chem. A*, 2013, **1**, 63–67.

38 B. Soni, M. W. Schilling and B. Mahmoud, Transparent bio-nanocomposite films based on chitosan and TEMPO-oxidized cellulose nanofibers with enhanced mechanical and barrier properties, *Carbohydr. Polym.*, 2016, **151**, 779–789.

39 K. Gao, Z. Shao, X. Wang, Y. Zhang, W. Wang and F. Wang, Cellulose nanofibers/multi-walled carbon nanotube nano-hybrid aerogel for all-solid-state flexible supercapacitors, *RSC Adv.*, 2013, **3**, 15058–15064.

40 X. Yang, L. Zhao and J. Lian, Arrays of hierarchical nickel sulfides/MoS_2 nanosheets supported on carbon nanotubes backbone as advanced anode materials for asymmetric supercapacitor, *J. Power Sources*, 2017, **343**, 373–382.

41 R. K. Mishra, A. K. Kushwaha, S. Kim, S. G. Seo and S. H. Jin, Vertical-slate-like MoS_2 nanostructures on 3D-Ni-foam for binder-free, low-cost, and scalable solid-state symmetric supercapacitors, *Curr. Appl. Phys.*, 2019, **19**, 1–7.

42 N. M. Dang, W.-W. Zhao, S.-I. Yusa, H. Noguchi and K. Nakashima, Cobalt oxide hollow nanoparticles as synthesized by templating a tri-block copolymer micelle with a core–shell–corona structure: a promising anode material for lithium ion batteries, *New J. Chem.*, 2015, **39**, 4726–4730.

43 S. Aloqayli, C. Ranaweera, Z. Wang, K. Siam, P. Kahol, P. Tripathi, O. Srivastava, B. K. Gupta, S. Mishra and F. Perez, Nanostructured cobalt oxide and cobalt sulfide for flexible, high performance and durable supercapacitors, *Energy Storage Mater.*, 2017, **8**, 68–76.

44 M. Rosa, E. Medeiros, J. Malmonge, K. Gregorski, D. Wood, L. Mattoso, G. Glenn, W. Orts and S. Imam, Cellulose nanowhiskers from coconut husk fibers: Effect of preparation conditions on their thermal and morphological behavior, *Carbohydr. Polym.*, 2010, **81**, 83–92.

45 A. Diallo, A. Beye, T. B. Doyle, E. Park and M. Maaza, Green synthesis of Co_3O_4 nanoparticles via Aspalathus linearis: physical properties, *Green Chem. Lett. Rev.*, 2015, **8**, 30–36.

46 B. Abu-Zied and S. Soliman, Nitrous oxide decomposition over $MCO_3–$ Co_3O_4 (M = Ca, Sr, Ba) catalysts, *Catal. Lett.*, 2009, **132**, 299.

47 N. D. Wanasekara, A. Michud, C. Zhu, S. Rahatekar, H. Sixta and S. J. Eichhorn, Deformation mechanisms in ionic liquid spun cellulose fibers, *Polymer*, 2016, **99**, 222–230.

48 N. Padmanathan, S. Selladurai and K. M. Razeeb, Ultra-fast rate capability of a symmetric supercapacitor with a hier-

archical Co$_3$O$_4$ nanowire/nanoflower hybrid structure in non-aqueous electrolyte, *RSC Adv.*, 2015, **5**, 12700–12709.

49 B. Fan, Q. Yao, C. Wang, Y. Xiong, Q. Sun and C. Jin, Spawns Structure of Rod-Like ZnO Wrapped in Cellulose Nanofibers for Electromagnetic Wave Absorption, *J. Nanomater.*, 2017, **2017**, 6329072.

50 G. Wang, H. Wang, Y. Ling, Y. Tang, X. Yang, R. C. Fitzmorris, C. Wang, J. Z. Zhang and Y. Li, Hydrogen-treated TiO2 nanowire arrays for photoelectrochemical water splitting, *Nano Lett.*, 2011, **11**, 3026–3033.

51 Q. Huang, J. Zhang, Z. He, P. Shi, X. Qin and W. Yao, Direct fabrication of lamellar self-supporting Co$_3$O$_4$/N/C peroxy-monosulfate activation catalysts for effective aniline degradation, *Chem. Eng. J.*, 2017, **313**, 1088–1098.

52 C. Wang, C. Zhang, W. Hua, Y. Guo, G. Lu, S. Gil and A. Giroir-Fendler, Catalytic oxidation of vinyl chloride emissions over Co-Ce composite oxide catalysts, *Chem. Eng. J.*, 2017, **315**, 392–402.

53 X. Lu, X. Huang, S. Xie, T. Zhai, C. Wang, P. Zhang, M. Yu, W. Li, C. Liang and Y. Tong, Controllable synthesis of porous nickel–cobalt oxide nanosheets for supercapacitors, *J. Mater. Chem.*, 2012, **22**, 13357–13364.

54 M. Gao, W.-K. Wang, Q. Rong, J. Jiang, Y.-J. Zhang and H.-Q. Yu, Porous ZnO-coated Co$_3$O$_4$ nanorod as a high-energy-density supercapacitor material, *ACS Appl. Mater. Interfaces*, 2018, **10**, 23163–23173.

55 M. Liao, Y. Liu, Z. Hu and Q. Yu, Novel morphologic Co$_3$O$_4$ of flower-like hierarchical microspheres as electrode material for electrochemical capacitors, *J. Alloys Compd.*, 2013, **562**, 106–110.

56 X.-C. Dong, H. Xu, X.-W. Wang, Y.-X. Huang, M. B. Chan-Park, H. Zhang, L.-H. Wang, W. Huang and P. Chen, 3D graphene–cobalt oxide electrode for high-performance supercapacitor and enzymeless glucose detection, *ACS Nano*, 2012, **6**, 3206–3213.

57 X. Wang, M. Li, Z. Chang, Y. Yang, Y. Wu and X. Liu, Co$_3$O$_4$@ MWCNT nanocable as cathode with superior electrochemical performance for supercapacitors, *ACS Appl. Mater. Interfaces*, 2015, **7**, 2280–2285.

58 A. K. Singh, D. Sarkar, K. Karmakar, K. Mandal and G. G. Khan, High-performance supercapacitor electrode based on cobalt oxide–manganese dioxide–nickel oxide ternary 1D hybrid nanotubes, *ACS Appl. Mater. Interfaces*, 2016, **8**, 20786–20792.

59 S. S. Karade and B. R. Sankapal, Two dimensional crypto-melane like growth of MoSe$_2$ over MWCNTs: symmetric all-solid-state supercapacitor, *J. Electroanal. Chem.*, 2017, **802**, 131–138.

60 K. Singh, S. Kumar, K. Agarwal, K. Soni, V. R. Gedela and K. Ghosh, Three-dimensional graphene with MoS$_2$ nanohybrid as potential energy storage/transfer device, *Sci. Rep.*, 2017, **7**, 1–12.

61 D.-W. Wang, F. Li and H.-M. Cheng, Hierarchical porous nickel oxide and carbon as electrode materials for asymmetric supercapacitor, *J. Power Sources*, 2008, **185**, 1563–1568.

62 K. Xu, W. Li, Q. Liu, B. Li, X. Liu, L. An, Z. Chen, R. Zou and J. Hu, Hierarchical mesoporous NiCo$_2$O$_4$@MnO$_2$ core–shell nanowire arrays on nickel foam for aqueous asymmetric supercapacitors, *J. Mater. Chem. A*, 2014, **2**, 4795–4802.

63 X. Lu, M. Yu, T. Zhai, G. Wang, S. Xie, T. Liu, C. Liang, Y. Tong and Y. Li, High energy density asymmetric quasi-solid-state supercapacitor based on porous vanadium nitride nanowire anode, *Nano Lett.*, 2013, **13**, 2628–2633.

64 P. Howli, S. Das, S. Sarkar, M. Samanta, K. Panigrahi, N. S. Das and K. K. Chattopadhyay, Co$_3$O$_4$ nanowires on flexible carbon fabric as a binder-free electrode for all solid-state symmetric supercapacitor, *ACS Omega*, 2017, **2**, 4216–4226.

65 X.-F. Lu, D.-J. Wu, R.-Z. Li, Q. Li, S.-H. Ye, Y.-X. Tong and G.-R. Li, Hierarchical NiCo$_2$O$_4$ nanosheets@hollow micro-rod arrays for high-performance asymmetric super-capacitors, *J. Mater. Chem. A*, 2014, **2**, 4706–4713.

66 Y. An, Y. Yang, Z. Hu, B. Guo, X. Wang, X. Yang, Q. Zhang and H. Wu, High-performance symmetric supercapacitors based on carbon nanosheets framework with graphene hydrogel architecture derived from cellulose acetate, *J. Power Sources*, 2017, **337**, 45–53.

67 K. Karthikeyan, D. Kalpana, S. Amaresh and Y. S. Lee, Microwave synthesis of graphene/magnetite composite electrode material for symmetric supercapacitor with superior rate performance, *RSC Adv.*, 2012, **2**, 12322–12328.

68 Z. Lei, J. Zhang and X. Zhao, Ultrathin MnO$_2$ nanofibers grown on graphitic carbon spheres as high-performance asymmetric supercapacitor electrodes, *J. Mater. Chem.*, 2012, **22**, 153–160.

69 T. S. Mathis, N. Kurra, X. Wang, D. Pinto, P. Simon and Y. Gogotsi, Energy storage data reporting in perspective—guidelines for interpreting the performance of electro-chemical energy storage systems, *Adv. Energy Mater.*, 2019, **9**, 1902007.

70 Q. Wei, Y. Jiang, X. Qian, L. Zhang, Q. Li, S. Tan, K. Zhao, W. Yang, Q. An and J. Guo, Sodium ion capacitor using pseudocapacitive layered ferric vanadate nanosheets cathode, *iScience*, 2018, **6**, 212–221.

71 V. Kuzmenko, N. Wang, M. Haque, O. Naboka, M. Flygare, K. Svensson, P. Gatenholm, J. Liu and P. Enoksson, Cellulose-derived carbon nanofibers/graphene composite electrodes for powerful compact supercapacitors, *RSC Adv.*, 2017, **7**, 45968–45977.

72 L. Zhang, P. Zhu, F. Zhou, W. Zeng, H. Su, G. Li, J. Gao, R. Sun and C.-P. Wong, Flexible asymmetrical solid-state supercapacitors based on laboratory filter paper, *ACS Nano*, 2016, **10**, 1273–1282.

73 X. Lu, Y. Zeng, M. Yu, T. Zhai, C. Liang, S. Xie, M. S. Balogun and Y. Tong, Oxygen–deficient hematite nanorods as high–performance and novel negative electro-des for flexible asymmetric supercapacitors, *Adv. Mater.*, 2014, **26**, 3148–3155.

74 L. Wang, H. Yang, X. Liu, R. Zeng, M. Li, Y. Huang and X. Hu, Constructing hierarchical tectorum–like α–Fe$_2$O$_3$/

PPy nanoarrays on carbon cloth for solid–state asymmetric supercapacitors, *Angew. Chem., Int. Ed.*, 2017, **56**, 1105–1110.

75 J.-X. Feng, S.-H. Ye, X.-F. Lu, Y.-X. Tong and G.-R. Li, Asymmetric paper supercapacitor based on amorphous porous Mn_3O_4 negative electrode and $Ni(OH)_2$ positive electrode: a novel and high-performance flexible electrochemical energy storage device, *ACS Appl. Mater. Interfaces*, 2015, **7**, 11444–11451.